Earth and Planetary Science Letters 497 (2018) 12–21

Contents lists available at ScienceDirect

Earth and Planetary Science Letters

www.elsevier.com/locate/epsl

Comparing dune migration measured from remote sensing with sand flux prediction based on weather data and model, a test case in Qatar

Sylvain Michel [a,b,*], Jean-Philippe Avouac [a], François Ayoub [a], Ryan C. Ewing [c], Nathalie Vriend [d], Essam Heggy [e,f]

[a] California Institute of Technology, Department of Geology and Planetary Sciences, 1200 E California Blvd, Pasadena, CA, 91125, USA
[b] University of Cambridge, Department of Earth Sciences, Bullard Laboratories, Madingley Road, Cambridge, Cambridgeshire, CB3 0EZ, UK
[c] Texas A&M University, Department of Geology and Geophysics, 3115 TAMU, College Station, TX, 77843, USA
[d] University of Cambridge, Department of Applied Mathematics and Theoretical Physics, Cambridge, Cambridgeshire, CB3 0WA, UK
[e] University of Southern California, Viterbi School of Engineering, 3650 McClintock Ave, Los Angeles, CA, 90089, USA
[f] Jet Propulsion Laboratory, California Institute of Technology, 4800 Oak Grove Dr, Pasadena, CA, 91109, USA

A R T I C L E I N F O

Article history:
Received 23 January 2018
Received in revised form 7 May 2018
Accepted 21 May 2018
Available online 15 June 2018
Editor: A. Yin

Keywords:
dunes dynamics
wind
remote sensing
planetary geomorphology
global circulation model

A B S T R A C T

This study explores validating and calibrating the wind regime predicted by Global Circulation Models (GCM) on Earth and other planets using optical remote sensing of dune dynamics. We use Spot-5 images to track the migration of 64 Barchan dunes in Qatar using the COSI-Corr technique. We estimate the volume of the dunes using a scaling law calibrated from one particular dune, which was surveyed in the field. Using volume and migration rate, we determine the sand flux from a single dune, Q_{Dunes}, and scale this estimate to the whole dune field. We compare the measured sand flux with those derived from wind velocity measurements at a local meteorological station as well as with those predicted from ERA-Interim (a Global Circulation Model). The comparison revealed that the wind velocity predicted by ERA-Interim is inappropriate to calculate the sand flux. This is due to the 6-h sampling rate and to systematic bias revealed by a comparison with the local wind data. We describe a simple procedure to correct for these effects. With the proposed correction, similar sand flux are predicted using the local and ERA-Interim data, independently of the value of the value of the shear velocity threshold, u_{*t}. The predicted sand flux is about 65% of Q_{Dunes}. The agreement is best assuming the value $u_{*t} = 0.244$ m/s, which is only slightly larger than the value of $u_{*t} = 0.2612$ m/s estimated based in the sand granulometry measured from field samples. The influence of the dune topography on the wind velocity field could explain the underestimation. In any case, the study demonstrates the possibility of validating GCM model and calibrating aeolian sand transport laws using remote sensing measurements of dune dynamics and highlights the caveats associated to such an approach.

1. Introduction

Dune fields are among the most prominent geomorphological features of arid environments on Earth. Their morphological, granulometric and compositional characteristics as well as their dynamics provide crucial insight into the geological and climatic conditions that led to their formation. Dune fields are also common geomorphological features of a number of extraterrestrial bodies such as Mars, Venus and Titan (Anderson et al., 1999; Ayoub et al., 2014; Bourke et al., 2008; Ewing et al., 2015a; Greeley and Iversen, 1985; Lorenz, 2006; McDonald et al., 2016; Tsoar et al., 1979). Their morphodynamics hold clues regarding climate and landscape evolution on these planetary bodies. One approach to investigate dune dynamics consists of comparing the observed geometry and dynamics of aeolian bedforms with sand flux predicted from General Circulation Models (GCM) (Ayoub et al., 2014; Bridges et al., 2012; Newman et al., 2017). While common, in practice, a number of factors hinder the accuracy of this approach. For example, Ayoub et al. (2014) measured seasonal variations of bedforms migration rates at Nili Patera, Mars, and could reproduce these variations based on a Mars GCM by adjusting the wind speed threshold for sand motion. The physical significance of the threshold obtained from that study is, however, unclear as it combines the threshold needed to initiate sand motion and

* Corresponding author at: California Institute of Technology, Department of Geology and Planetary Sciences, 1200 E California Blvd, Pasadena, CA, 91125, USA.
E-mail addresses: sylvain_michel@live.fr (S. Michel), avouac@gps.caltech.edu (J.-P. Avouac), fayoub@gps.caltech.edu (F. Ayoub), rce@tamu.edu (R.C. Ewing), nv253@cam.ac.uk (N. Vriend), heggy@usc.edu (E. Heggy).

https://doi.org/10.1016/j.epsl.2018.05.037
0012-821X/

the much lower threshold needed to sustain saltation (Kok, 2010; Sullivan and Kok, 2017; Yizhaq et al., 2014). Moreover, the threshold that was determined for a wind regime does not account for near surface turbulence, which is critical in driving sand motion (Martin et al., 2013). Indeed, some GCMs are not able to resolve localized interference, either due to the fact that it does not account for topographic features that would influence the wind's direction and strength (Jackson et al., 2015), or either due to low time resolution that does not account for high frequency changes of wind strength and direction (Barchyn et al., 2014; Martin et al., 2013). Although resolved at higher spatial resolutions than GCMs, regional wind models may not be accurate enough either to determine local sand fluxes over a dune and through a dune field (Jackson et al., 2015). This raises the question as to whether climate models can represent winds accurately enough to predict sand fluxes.

Aeolian transport laws used to predict sand flux (Bagnold, 1941; Martin and Kok, 2017; White, 1979) are based on necessary simplifications that might hinder the accuracy of the forecast. For example, aeolian sand transport can result from saltation or reptation (Anderson et al., 1991; Andreotti, 2004; Lammel et al., 2012). A particle in saltation, or 'salton', corresponds to a high kinetic energy grain ejected from the surface that will have enough energy to eject further particles when it impacts the sand bed again, whereas a particle in reptation, or 'repton', is a low kinetic energy grain that will hop without moving any other sand grain at its impact with the surface (Anderson et al., 1991; Andreotti, 2004; Bagnold, 1941). However, transport laws only account for saltons and the relative contribution of reptons and saltons to the total sand flux involved in migration of bedforms of particular scale, ripples or dunes for example, are little considered (Butterfield, 1999). In addition, empirical transport laws are typically obtained for transport over flat surface at sand saturated conditions and do not consider bedform topography or sediment availability-limited scenarios. This makes comparison of model predictions with nature difficult and highlights the need for calibration. Potentially, a scale-dependent correction factor might need to be applied when a given transport law is used. In this study, we address the issue of sand flux prediction discrepancy obtained from GCMs and surface measurements. We selected a sand dune field site in Qatar for its simple geographic setting. We measured dune migration using the COSI-Corr technique (Leprince et al., 2007) applied to a time series of optical images and compared the observation with wind velocity measured from a local station and predicted from a GCM. We used the GCM ERA-Interim (Dee et al., 2011), as well as data from a meteorological station to assess ways of correcting the GCM predictions for near-surface wind turbulence.

2. Dunes migration and estimated sand flux at the study site in Qatar

Before focusing on sand flux prediction from meteorological data, we estimate sand fluxes from field measurements and remote sensing data. Those results serve as point of comparison with weather-based predictions and provide an estimation of their accuracy.

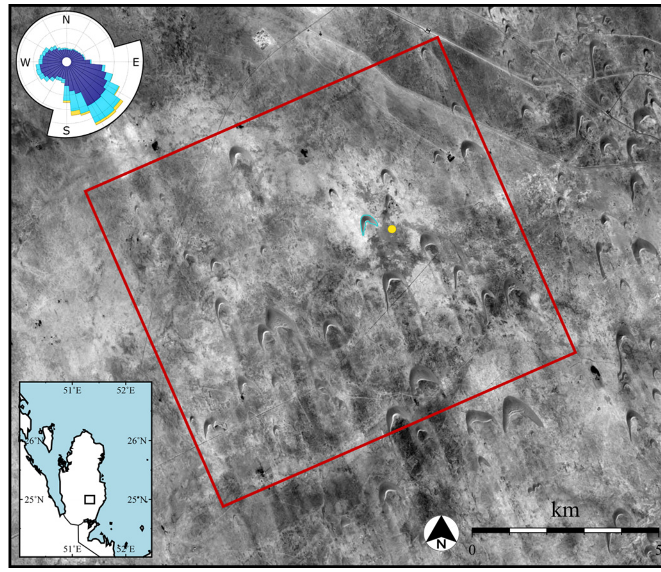

Fig. 1. Regional setting. The red square represents our area of study. The yellow dot is the location of the meteorological station. The dune surrounded in blue corresponds to the one we have computed a DEM for. The wind rose at the upper left corner of the figure indicates dominating winds going to the SE. Dark blue, light blue and yellow histograms of the wind rose indicate the percentage of wind under 5 m/s, between 5–10 m/s, and over 10 m/s, respectively. (For interpretation of the colors in the figure(s), the reader is referred to the web version of this article.)

2.1. Setting of study area in Qatar

The study area is a barchan dune field located in southeastern Qatar (Fig. 1). The region is dominantly affected by the Shamal, a unidirectional wind coming from the NW, which is stronger in winter and summer (Edgell, 2006). The lithographic unit of the exposed bedrock of Qatar is almost exclusively carbonates (e.g., limestone and dolomite). The topography is flat for most of Qatar, with a slight north-south anticline located on the west side of the dune field, which rises to ∼103 m above sea level. The very simple general setting of this region makes it a perfect case study for our test. The dune mineralogy indicates that the sand source does not come from Qatar, delimited as it is now, but from sediments now laying under the Persian sea that were previously exposed during a Pleistocene sea-level low stand (Embabi and Ashour, 1993; Garzanti et al., 2013). The sediment itself originates from the Zagros region (Garzanti et al., 2013). This source was cut off around 8000–12000 years ago, when the Persian Gulf was flooded due to the sea level rise at the beginning of the latest inter-glacial period (Lambeck, 1996). We focus on the upwind dunes located on the NW end of the dune field (Fig. 1). The study area is about 8.4 10^4 km^2 and contains 64 SE migrating dunes, with widths between 55 and 808 m.

2.2. Remote sensing analysis

The average migration velocities of the 64 dunes were estimated from the comparison of the dunes locations on two SPOT5 images (Table 1), with a ground sampling distance of 2.5 m, acquired 10 yr apart in 2003 and 2013. The two satellite images were orthorectified and accurately coregistered using the Co-registration

Table 1
Optical images data set.

Satellite	Acquisition date	Time (UTC)	Spectral band	Resolution	Incidence angle
SPOT 5	22 Mai 2003	07:23:11.9	Panchromatic	2.5 m	0.8°
SPOT 5	02 April 2013	07:11:53.4	Panchromatic	2.5 m	23.3°

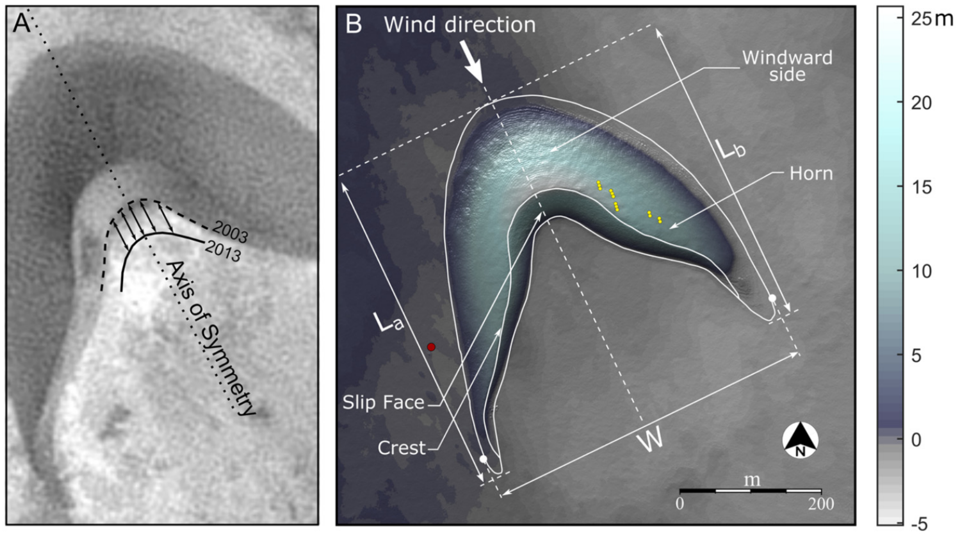

Fig. 2. Dune displacement measurement method, characterization of a dune's geometrical feature and DEM of the dune highlighted in Fig. 1. (A) Spot5 satellite image taken on the 22nd of May 2003. The black dashed and solid line correspond to the outline of the dune leefront toe in 2003 and 2013, respectively. The arrows show examples of the dune displacement measurements, which are taken parallel to the dune axis of symmetry (dotted black line). (B) Characterization of a dune's geometrical feature and DEM of the dune highlighted in Fig. 1. The red dot shows the reference point for the calculation of the DEM (all elevations and distances are calculated relative to this point). The yellow dots indicate the location of the sand samples.

of Optically Sensed Images and Correlation (COSI-Corr) methodology (Leprince et al., 2007). The misregistration error after co-registration is about 70 cm. The migration velocity of each of the 64 dunes was estimated from measuring the distance between the toe of their slip faces between the two co-registered satellite images (Fig. 2A). The measurements were done along the transport direction indicated by the axis of symmetry of each dune. The mean azimuth of transport is of $156.64 \pm 4.07°$E. To alleviate measurement uncertainties, about 10 measurements per dune were collected. The dunes velocities range from 2.48 ± 0.79 m/yr to 27.46 ± 0.17 m/yr, the velocity decreasing with increasing dune size. Those measurements are consistent with those estimated by Louge et al. (2013).

In order to verify the inverse relationship between dune size and migration velocity, we measured the geometrical characteristics, width and length of all the dunes using a high resolution satellite image (Digitalglobe satellite with resolution between 1.24–1.85 m) taken on the 2nd of February 2015 available on Google Earth. The mean and standard deviation of the width of each dune were also estimated by measuring 10 times these parameters at various locations along the front of the dune.

Our data (Fig. 3) follow approximately the relationship between the migration velocity, C, and the dune's width, W, of Hersen et al. (2004), who proposed,

$$\frac{1}{C} = \frac{W}{A} + B. \tag{1}$$

Using the linear regression method of York et al. (2004), which takes into account the uncertainties on both width and velocity, we determine the constant to $A = 2224 \pm 47$ m^2/yr and $B = 1.210^{-2} \pm 1.710^{-3}$ yr/m. The mean residence time of a sand grain within a moderate sized dune (i.e. indicated dune in Fig. 1; $W = 467$ m) is estimated to $\sim$37.5 years using the method of Zhang et al. (2014).

2.3. Field investigations

We surveyed a dune (outlined in blue in Fig. 1) located approximately 500 m from a weather station (yellow dot in Fig. 1). A high resolution (0.6 m/pixel) Digital Elevation Model (DEM) of the dune was obtained from structure-from-motion (sfm) applied to a set of images that we acquired using an Unmanned Airborne Vehicle

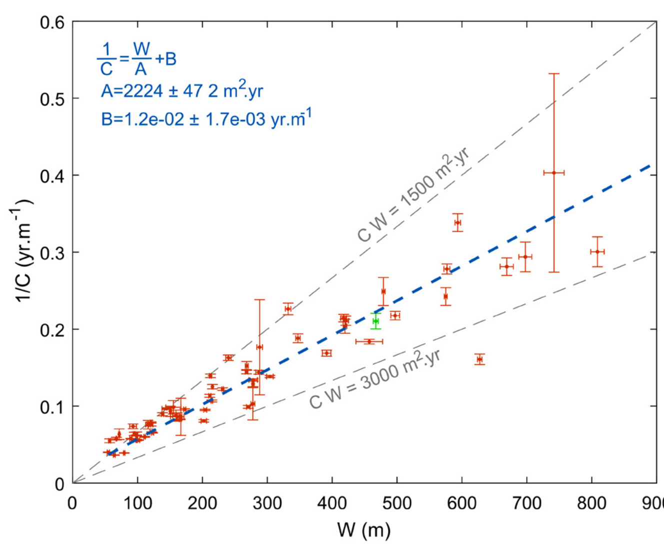

Fig. 3. Comparison between dune's velocity, C, and dune's width, W. A linear correlation between $1/C$ and W is observed. The best fitting law is determined with the linear regression method (York et al., 2004) which allows taking into account the uncertainties on width and speed. The green dot and errorbars corresponds to the dune indicated in Fig. 1.

(UAV) (Fig. 2B) (Supplement Information). The topography of the upper portion of the dune is well resolved, but the lower portion less so due to the lack of texture (we notice a slight depression in the DEM, which indicates a local bias of the order of $\sim$0.5 m). The bedrock topography under the dune is estimated from interpolation of the surrounding bedrock topography using a Delaunay triangulation method. The volume of the dune is estimated to 848,966 m^3. The DEM bias in areas of low texture amount to a total dune volume bias of the order of $\sim$1% and is neglected. The main source of error is due to the interpolation of the bedrock topography.

Thirteen sand samples were collected at different locations (Fig. 2B) within the blue outlined dune in Fig. 1. The sand ranged in size from fine to medium with a median size for all samples of 236 μm (Supplementary). Samples ranged from very well sorted to well sorted (Supplementary).

2.4. Estimated sand flux

We estimate the sand flux at the scale of a single dune, Q_{Dunes}, and the sand flux at the scale of the dune field, Q_{Field} (Ould Ahmedou et al., 2007). Q_{Dunes} is defined as the dune's mass of sand, transported through a width W at the speed C. The average value once the dune has migrated over a distance equal to its length along transport direction, L is given by,

$$Q_{Dunes} = \frac{(1-\phi)\rho_s V C}{W L}, \tag{2}$$

where ϕ is the porosity of the dune, ρ_s the volumic mass density of sand grains (2700 $\mathrm{kg\,m^{-3}}$), V the volume of the dune (in $\mathrm{m^3}$), C the dune velocity (in $\mathrm{m\,yr^{-1}}$), W the dune's width (in m) and L the mean length of the dune (in m) (Ould Ahmedou et al., 2007). We assume a porosity of 36% (Louge et al., 2010). The mean length is determined by

$$L = \frac{L_a + L_b}{2}, \tag{3}$$

with L_a and L_b the lengths of the dune measured respectively from both dune's horns (Fig. 2). Given the homogeneity of the sand characteristics, topographic and climatic setting in the study area, we assume that all the dunes have a similar scale-independent shape. The volume of each dune can then be estimated using a scaling law, $V = K * W^3$ (Durán et al., 2010; Hersen et al., 2004). The constant K is calibrated to 8.33 10^{-3} from the estimated volume of the dune which was surveyed in the field.

The average Q_{Dunes} estimated from the 64 dunes considered in this study is estimated to 24,559 $\pm$ 6895 $\mathrm{kg\,m^{-1}\,yr^{-1}}$.

Q_{Field} takes into account the density of dunes distribution and is estimated using the equation

$$Q_{Field} = (1-\phi)\rho_s \sum_{i=1}^{T} \frac{C_i V_i}{W_f L_f}, \tag{4}$$

with C_i and V_i the velocity and volume of dune i, and W_f and L_f the width and length of the dune field (Ould Ahmedou et al., 2007). Q_{Field} is estimated to 2,569 $\mathrm{kg\,m^{-1}\,yr^{-1}}$. The density of the dune field seems relatively low, hinting for high sediment loss (Génois et al., 2013).

3. Sand flux prediction using meteorological data and GCM models

In this section, we present the meteorological data from the local stations and compare with the predictions from a Global Circulation Model, ERA-Interim. We next discuss how sand flux predictions can be estimated based on such data and compare with the results from our remote sensing analysis.

3.1. Meteorological data

We used data from a meteorological station located in the dune field (courtesy of Michel Louge) (yellow dot in Fig. 1). The instruments on site include an anemometer, at 2.52 m and a weather vane. We use 2 yr of data acquired between 2012 and 2014 with an estimate of wind speed and direction recorded every minute and 10 min, respectively. We extrapolate linearly the wind direction in time to have also a value for every minute. The wind speed ranges between 0 and 16 m/s and is blowing mostly to the SE with some variation during the year (wind rose in Fig. 1). Note that the instruments on site have undergone a bias. The mast of the installation has been rotating gradually to the West throughout the years. This shift in azimuth is assumed to be linear in time and the wind direction has been consequently corrected for it (Supp.).

We compared the local meteorological data with the predictions from ERA-Interim (Dee et al., 2011). ERA-Interim is a global atmospheric model, which is refined with a post-assimilation of measurements from meteorological stations and other miscellaneous sources. It combines measurements and physical assumptions to compute a global best estimate of various atmospheric and oceanic parameters. We chose ERA-Interim because of its higher spatial resolution relative to other reanalysis products (NCEP/NCAR in particular). The sampling frequency is one sample per 6 h, and each sample corresponds to an average over this time period. We used the wind speed and direction at 10 m height predicted by the model. Given the 80 km post-spacing of ERA-Interim grid, we consider the ERA-Interim value at that closest grid point for comparison with the station. The closest point from the ERA-Interim model grid to the meteorological station is located at $\sim$3.7 km in the SE direction.

Fig. 4 shows examples of wind velocity variations through time and the effect of time averaging. In this region, the wind is dominated by daily variation with stronger winds during the day (Fig. 5A). Shorter period variation can also be observed but account for lower amplitude (Fig. 5A). Seasonal variations are not clearly observed between 2012 and 2014.

We observe significant differences between ERA-Interim's and the 6-h average meteorological station data (Fig. 5). The wind velocity extracted from ERA-Interim's is underestimated during periods of very low wind velocity ($u_* < 0.075$ m/s), overestimated during periods of low to medium wind velocity ($0.075 < u_* <$ 0.29 m/s) and, underestimated during periods of high wind velocity (0.29 m/s $< u_*$) (Fig. 5B and C). The difference between the GCM prediction and the local measurements of wind velocity also shows up in the comparison of their amplitude spectra (Fig. 5A). Both show a dominant diurnal cycle, which is clearly visible in Fig. 4. However, the amplitude of this cycle is smaller by 35% for ERA-Interim. Averaging over a time period longer than 6 h would smooth the diurnal variations and wind bursts that are the main cause of sand displacement. This analysis makes evident that the diurnal variations of the wind velocities and stochastic variations at the sub-daily scale need to be accounted for to estimate the sand flux.

3.2. Methodology for sand transport law calibration

The effect of wind on the sand flux is generally expressed as a function of wind shear velocity (or friction velocity), u_*. The wind velocity itself is linked to u_* via the law-of-the-wall, which describes the wind speed gradient profile and is given by

$$u(z) = \frac{u_*}{\kappa} \ln\left(\frac{z}{z_0}\right) \quad \text{for } z \geq z_0 \tag{5}$$

where u is the wind speed at height z, κ is the Von Karman constant ($\kappa = 0.4$), and z_0 is the aerodynamic roughness height (Bagnold, 1941). The wind velocity decreases as you get closer to the surface and reaches 0 at the height z_0.

It is generally considered that sand flux at large scale (i.e. dunes) is dominated by saltation. Even though reptation seems to play a significant role at very high wind speed (Lammel et al., 2012), we are assuming that saltation is the major transport mode.

Many sand flux laws are available from the literature and mostly describe a saltation-only saturated sand flux (usually given in $\mathrm{kg\,m^{-1}\,s^{-1}}$) for transport on a flat surface. We are using in this study the relation from White (1979), which is based on previous studies (Kawamura, 1951; White, 1979) which states

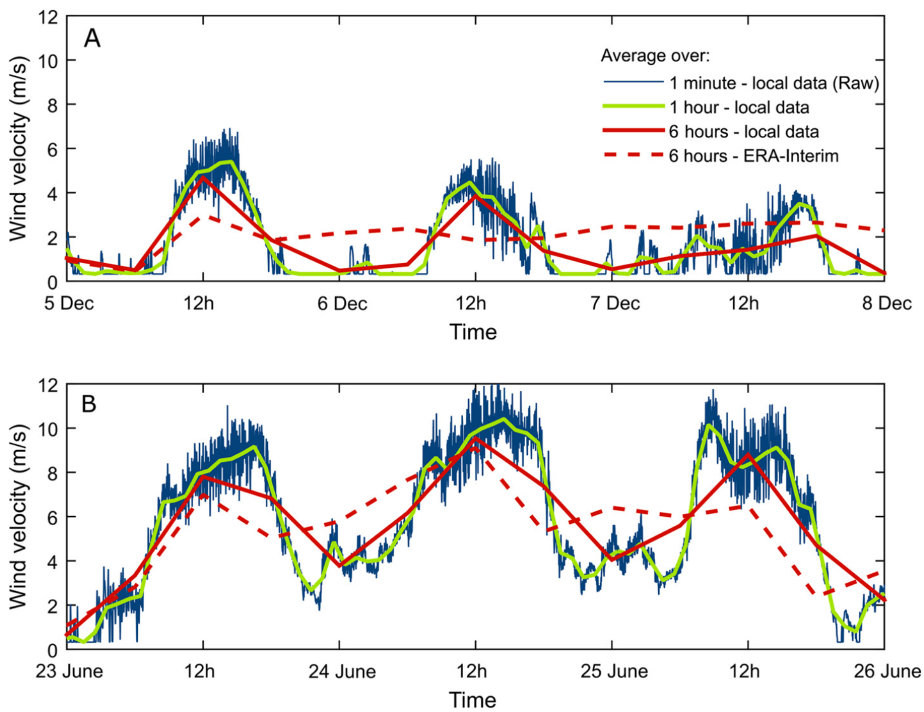

Fig. 4. Wind velocity at 2.52 m height for different time averaging of the meteorological station data and for ERA-Interim. We selected two contrasted periods in winter time (A) and summer time (B). ERA-Interim's curve was obtained using equation (5) to get 2.52 m height estimations from 10 m height data (see details in section 3.2). We chose $z_0 = 3D_p/30$, with $D_p = 236$ μm.

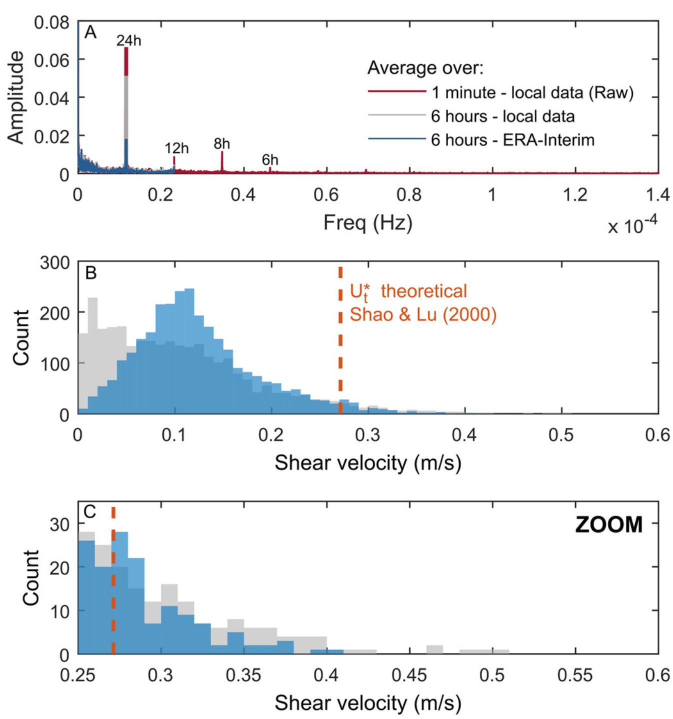

Fig. 5. Spectrum and histogram of the shear wind velocity. (A) Spectra of the shear wind velocity of the raw and 6-h averaged meteorological data and of ERA-Interim's data. (B) Histogram of the shear wind velocity of the 6-h averaged meteorological station and ERA-Interim's data. The vertical dashed orange line is Shao and Lu's (2000) shear velocity threshold for a mean sand diameter of 236 μm. (C) is a zoom of (B). It shows that the data from the 6-h averaged meteorological station is generally stronger than ERA-Interim's data for winds higher than the theoretical shear wind threshold from Shao and Lu (2000).

$$
\begin{aligned}
q_s &= C_W \frac{\rho_a}{g}\left(u_*^2 - u_{*t}^2\right)(u_* + u_{*t}) && \text{for } u_* > u_{*t} \\
q_s &= 0 && \text{for } u_* < u_{*t}
\end{aligned}
\tag{6}
$$

where u_{*t} is the shear velocity threshold (or impact threshold), ρ_a the air density, g the gravitational force and C_W a constant equal to 2.61. This law has been extensively used for planetary science (i.e. Anderson et al., 1999; Ayoub et al., 2014; McDonald et al., 2016). u_{*t} can be described as the shear velocity at which effective saltation transport is sustained. The sand flux is assumed null when the shear wind velocity is less than u_{*t}.

The parameters u_{*t} and u_* are actually mutually dependent because they both depend on the mean size particle D_p. On one hand, u_* is a function of $z_0 = k_s/30$ (White, 2006) where k_s is the Nikuradse roughness (Nikuradse, 1933). For monodisperses spherical particles in a homogeneous bed, Bagnold found that $k_s \approx D_p$ (Bagnold, 1941) with D_p the particles diameter. For more complex irregular surface of mixed sand, k_s ranges from two to five time the median particle diameter (Kok et al., 2012). On the other hand, the parameter u_{*t} is linked to the mean size particle D_p through the equation

$$
u_{*t} = A_N \sqrt{\frac{\rho_s - \rho_a}{\rho_a} g D_p + \frac{\gamma}{\rho_a D_p}}, \tag{7}
$$

where A_N is a dimensionless parameter equal to 0.111 and ρ_s is the volumetric mass density of sand (in $\mathrm{kg\,m^{-3}}$) (Shao and Lu, 2000). The interparticle forces are integrated using the parameter γ which ranges between 1.65×10^{-4} and 5×10^{-4} N/m. We chose $\gamma = 2.9\ 10^{-4}$ N/m (Kok et al., 2012; Kok and Renno, 2006).

Assuming a mean grain size of 236 μm, we get $u_{*t} = 0.2612$ m/s for our study area.

The appropriate shear velocity threshold u_{*t} for a particular area is often unknown as it depends on local parameters (D_p or z_0). Several options are available to calibrate its value using remote sensing data and weather data. One possible option consists in comparing the amplitude of the seasonal variations of the sand flux with the prediction based on the weather data (e.g., Ayoub et al., 2014). This approach is not possible here as we have no observational constraints on the temporal variations of the sand flux.

A second option is to calibrate it using the mean azimuth (Ewing et al., 2015b; McDonald et al., 2016). The wind azimuth changes through the year and has often a seasonal preferential direction and strength. For example, low wind speeds ($u_* < u_{*t}$) might have a different azimuth than the stronger wind speeds ($u_* > u_{*t}$). The mean azimuth calculated from a GCM would consequently change depending on the value of u_{*t} and the correct wind shear threshold will then give a mean azimuth equal to the azimuth of the dunes. The advantage of these two approaches is that the determination of u_{*t} is independent of the pre-factor of the sand transport law (equation (6)). A third approach consists in comparing the observed mean sand flux over a given period of time, $\overline{Q_s}$, with that predicted based on the meteorological data and the sand transport.

Here we test the second and third approaches. To do so, we need to calculate the mean sand flux $\overline{Q_s}$ (in kg$\dot{\mathrm{m}}^{-1}$ yr^{-1}) and the mean azimuth $\overline{\theta}$ (in degrees). Each wind speed at time step i is converted into u_* (equation (5)) and used to calculate the sand flux at this time, $q_{s,i}$. From the wind azimuth θ_i of each time step i, we can divide the sand flux $q_{s,i}$ into its North and East component, $\overrightarrow{q_{N,i}}$ and $\overrightarrow{q_{E,i}}$ respectively.

$$\begin{aligned}\overrightarrow{q_{E,i}} &= q_{s,i} * \cos(\theta_i)\\ \overrightarrow{q_{N,i}} &= q_{s,i} * \sin(\theta_i)\end{aligned} \tag{8}$$

The mean sand flux is given by

$$\overline{Q_s} = \frac{\sqrt{(\sum_{i=1}^{N} \overrightarrow{q_{N,i}})^2 + (\sum_{i=1}^{N} \overrightarrow{q_{E,i}})^2}}{N}, \tag{9}$$

where N is the total number of time step. The mean azimuth $\overline{\theta}$ is then given by

$$\overline{\theta} = atan2\left(\frac{\sum_{i=1}^{N} \overrightarrow{q_{E,i}}}{N}, \frac{\sum_{i=1}^{N} \overrightarrow{q_{N,i}}}{N}\right), \tag{10}$$

where $atan2$ is the four-quadrant inverse tangent. Note that $\overline{\theta}$ is a weighted mean azimuth because of the weighting by the wind speed.

$\overline{Q_s}$ and $\overline{\theta}$ are thus dependent on u_{*t}. As mentioned before, changing u_{*t} induces also to change D_p and z_0. Testing a certain u_{*t} involves testing a specific z_0 and D_p (equations (5) and (7)). The only free parameter is k_s.

The mean sand flux given by $\overline{Q_s}$ is presumably more comparable to Q_{Dunes} (section 2.4) since the flux is supposed to be saturated if we focus on one dune. On the other hand, Q_{Field} is dependent of the dune density on the field which is quite inhomogeneous in our study area. It represents nevertheless a minimum sand flux possible in the area.

3.3. Results

The attempt at calibrating u_{*t} using the sand flux mean azimuth is illustrated in Fig. 6. Using the raw meteorological data (thick blue full line), a change in wind shear velocity threshold induces a fluctuation on the mean azimuth of sand flux. The amplitude of this variation is limited to ~10 degrees and the distribution of the dune migration azimuths encloses those variations with values that span a range of ~20 degrees (gray histogram). Because of the small span of the predicted azimuth compared to the span of observed dune migration azimuth, the calibration is only very approximate. The calibrated value of u_{*t}, is obtained from the crossing of the mean azimuth of the dunes (thick dark gray dashed line) and the variation of the azimuth as a function of the shear velocity threshold. This would occur at $\sim 0.385 \pm 0.015$ m/s (yellow dot in Fig. 6), the uncertainty taken as the 1 sigma on the mean estimation, using the 1 min average data. This value

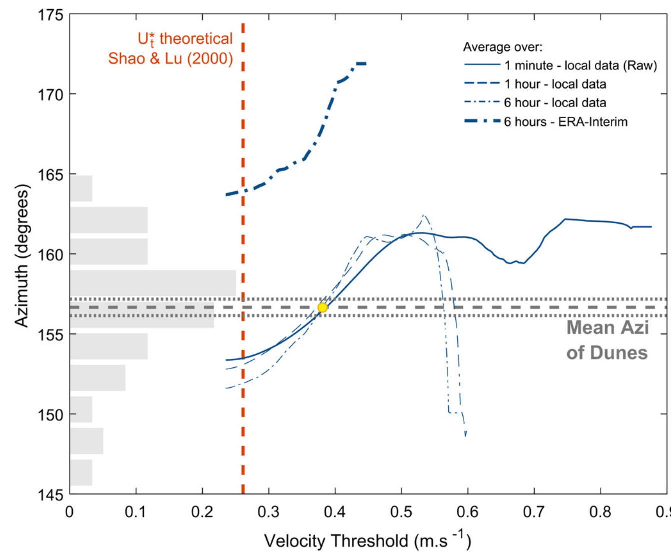

Fig. 6. Mean azimuths of sand flux, calculated from equation (10) using the data from the meteorological station and the wind velocity at 10 m height predicted by ERA-Interim, as a function of the shear velocity threshold. The histogram in grey represents the observed distribution of dune's symmetry axis (assumed to represent the mean azimuth or migration). The vertical dashed orange line is shear velocity threshold calculated with Shao and Lu's (2000) model for the mean sand diameter of 236 μm determined from a field sample. The horizontal grey dashed line represents the mean azimuth of the dunes. The horizontal grey dotted lines indicate the standard deviation on the mean azimuth of the dunes. The yellow dot indicates the point of comparison between the prediction (solid blue thin line) with the observation.

is significantly higher than the value of 0.26 m/s obtained from equation (7) based on the measured sand granulometry. Note that if we consider the hourly or 6-hourly averaged data, there is another crossing at $\sim 0.580 \pm 0.002$ m/s which is an artifact of the temporal-averaging (the uncertainty taken as the 1 sigma on mean estimation using the hourly average data). Additionally, the drift in azimuth experienced by the meteorological station mast might explain the calibration problem. The RMSE of the linear fit of the drift is equal to 5.8 degrees, which is equivalent to the difference between the azimuth estimation from equation (7) and the observed dunes migration azimuth.

When the wind velocity from ERA-Interim's is used, the sand flux azimuth variation (thick blue dashed line) is shifted by 10–15 degrees counter-clockwise compared to azimuth obtained with the meteorological station data. The predicted azimuth using the GCM's is inconsistent with the azimuth estimated from the dunes migration and the calibration is not possible. A possible bias in the wind velocity azimuth predicted by weather models should be considered if the azimuthal approach is used to calibrate the shear velocity threshold.

In any case, the calibration of u_{*t} based on the transport azimuth is not reliable in this study due to the small variations of the wind direction over the years. Barchan dunes are generally born and maintained from a mainly unidirectional wind and the azimuth calibration method is consequently not well suited for these type of dunes.

The results of the calibration of u_{*t} using the mean sand flux $\overline{Q_s}$ are shown in Fig. 7. The prediction based on the meteorological data at the original 1 min sampling rate for $k_s = 3\ D_p$ is represented by the thick blue continuous line. The shaded area represents the range of $\overline{Q_s}(u_{*t})$ with k_s spanning from D_p to 5 D_p. For a single u_{*t} over 0.23 m/s, the estimated sand flux has 2 solutions. This is a consequence of the interparticle forces integrated in equation (7). It indeed gets harder to initiate transport of very fine grains or dust due to the electrostatic forces. The model predicts a sand flux systematically lower than mean sand flux of a

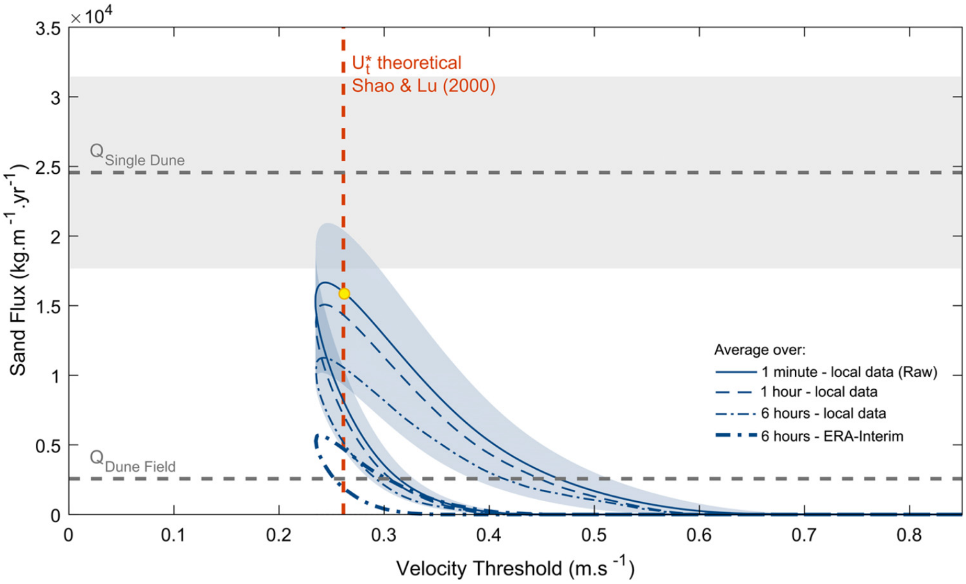

Fig. 7. Mean sand flux, calculated from equation (9) using the data from the meteorological station and the wind velocity at 10 m height predicted by ERA-Interim, as a function of the shear velocity threshold. The horizontal gray dashed line associated with $Q_{single\ dune}$ is the measured average sand flux for a single dune in our area (equation (2)). The shaded gray area represents its standard deviation. The horizontal gray dashed line associated with $Q_{Dune\ Field}$ is the measured sand flux of the dune field (equation (4)). The blue shaded area represents the possible range of the mean sand flux calculated with the data from the meteorological station at the original 1-min sampling rate and for a range of the Nikuradse constant, k_s, between 1 and 5. The vertical dashed orange line is shear velocity threshold calculated with Shao and Lu's (2000) model for the mean sand diameter of 236 μm determined from a field sample. The yellow dot indicates the point of comparison between the prediction (solid blue thin line) with the observation of $Q_{single\ dune}$.

single dune, Q_{Dunes}, whatever the choice of u_{*t}. The agreement is best for a value close to the minimum possible value of 0.23 m/s. For $u_{*t} = 0.26$ m/s, as estimated from equation (7) with the mean particle diameter of 236 μm, the predict sand flux is $\sim 1.6\ 10^4$ $\mathrm{kg\,m^{-1}\,s^{-1}}$, representing ∼65% of Q_{Dunes} (yellow dot in Fig. 7). By increasing k_s to $5D_p$, the predicted sand flux reaches ∼83% of Q_{Dunes}.

The sand flux predicted with the wind velocity extracted from ERA-Interim for $u_{*t} = 0.26$ m/s is only about 25% of Q_{Dunes}. This is an effect of the 6-h sampling rate and of the biased predictions described above. The GCM's sand flux estimate is indeed about 41% of the sand flux estimated based on the meteorological 6-h averaged local data. The 6-h averaging effect account only partly for the discrepancy as shown by the comparison with sand flux predicted based on the 6-h averaged local wind data. The GCM wind velocity predictions need therefore to be corrected.

A drift potential analysis is also presented in the supplement. It indicates the same trends in terms of averaging effects and differences between the meteorological station and ERA-Interim. The RDP/DP is in any case very high (>0.87), due to the mono-directionality of winds in Qatar.

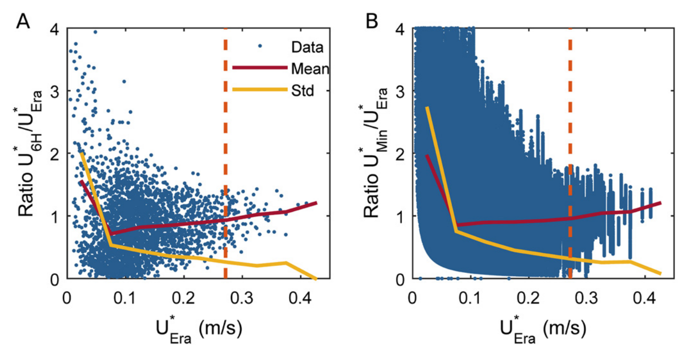

Fig. 8. Ratio between the shear wind velocity of the meteorological station and ERA-Interim's data as a function of the shear wind velocity of ERA-Interim. The blue dots represent the data. The red and yellow line correspond respectively to the ratio's mean and standard deviation as a function of U^*_{ERA}. The vertical dashed orange line is Shao and Lu's (2000) shear velocity threshold for a mean sand diameter of 236 μm. (A) The 6-h averaged meteorological station data is used in this panel to compute the ratio. (B) The raw meteorological station data is used in this panel to compute the ratio. Since ERA-Interim's data is a 6-h average of the wind speed, one point for U^*_{ERA} corresponds to several measurements from the raw meteorological data.

3.4. ERA-Interim's correction

As seen in Fig. 5, ERA-Interim is generally underestimating the wind velocity in Qatar for wind speeds over the shear velocity threshold, which leads to an underestimation of the mean sand flux. It is possible to stochastically correct this bias by looking at the ratio between the two sets of data. We will first take the example of ERA-Interim's correction with the 6-h averaged data from the meteorological station before also applying it to the raw data.

Each value of ERA-Interim's shear velocity, U^*_{ERA}, can be compared with the 6-h averaged data from the local meteorological station, U^*_{6h}. The ratio between the two datasets, $R = U^*_{6h}/U^*_{ERA}$, gives us information about the correction to apply. Fig. 8 shows the shear velocity ratio between the meteorological station and ERA-Interim's data as a function of ERA-Interim's shear wind speed, U^*_{ERA} (blue dots). We partitioned U^*_{ERA} into sections of 0.5 m/s and computed for each section the mean (red line) and standard deviation (yellow line) of the ratios. If the GCM's data were not biased, then the mean ratio should be equal to 1, independently of ERA-Interim's wind speed. Nevertheless, we observe a deviation from this ideal situation. For strong wind speed, the meteorological station velocities are higher than U^*_{ERA} $(R > 1)$. On the opposite, for low wind speed, the meteorological station velocities are weaker than U^*_{ERA} $(R < 1)$, except for very weak wind where the ratio shows much stronger meteorological station wind speed than ERA-Interim's. This trend is also visible in Fig. 5. Moreover, the standard deviation shows also a trend depending on ERA-Interim's shear velocity strength. The ratio between the two datasets are more dispersed for weak U^*_{ERA}, whereas stronger winds for the GCM implies less dispersion in R.

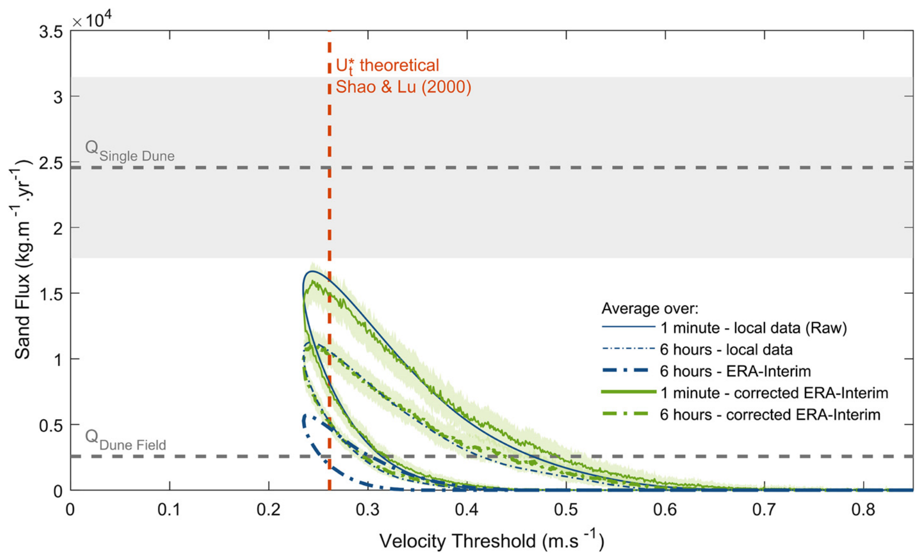

Fig. 9. ERA-Interim's sand flux correction. The blue lines correspond to the initial data and the green lines correspond to the ERA-Interim's sand flux correction. The green shaded area represents the standard deviation of the applied correction. The horizontal gray dashed line associated with $Q_{single\ dune}$ is the measured average sand flux for a single dune in our area (equation (2)). The shaded gray area represents its standard deviation. The horizontal gray dashed line associated with $Q_{Dune\ Field}$ is the measured sand flux of the dune field (equation (4)). The vertical dashed orange line is Shao and Lu's (2000) shear velocity threshold for a mean sand diameter of 236 µm.

To stochastically correct the sand flux from the GCM's data, two types of rectification needs to be applied to the friction velocity, one for the general trend observed from the ratios mean and one accounting for the dispersion of R.

From the partitioning of the data mentioned earlier, we suppose that within each section, the distribution of R follows a Normal distribution. The parameters of the Gaussian are set from the mean and standard deviation calculated in each section. Consequently, each value of ERA-Interim's shear velocity, U^*_{ERA}, is associated with a certain section and thus with a ratio's probability density given by the Normal distribution. For each U^*_{ERA}, we randomly sample a ratio from its associated probability density and correct its value applying

$$U^*_{ERA-Corr} = U^*_{ERA} R, \tag{11}$$

where $U^*_{ERA-Corr}$ is the corrected ERA-Interim's shear velocity. Applying this methodology will give us one solution, which will nevertheless be dependent on the fact that it is linked to the randomness of the sampling of the ratio. One needs then to apply this sequence several times to have multiple versions of the corrected shear velocity of ERA-Interim's data, from which a mean and standard deviation of the stochastically rectified sand flux can then be calculated (Fig. 9). Note that the correction is not wind-azimuth specific; we do not favor a specific wind direction.

The correction of U^*_{ERA} with the raw data from the meteorological station is slightly different. ERA-Interim's data is an average of the wind speed over 6 h, whereas the meteorological station raw data is an average over a minute. A value of shear velocity in ERA-Interim's data is thus associated with several values of the raw data shear velocity. Each point of ERA-Interim is associated 360 values of the minute averaged data from the local meteorological station, U^*_{Min}, and have consequently 360 values of R. Thus the more crowded plot in Fig. 8B. From thereon, the same partitioning of U^*_{ERA} into sections of 0.5 m/s is done and the same methodology is applied to correct U^*_{ERA}.

With these corrections, the sand flux predicted from the ERA-Interim wind velocity match remarkably well the sand flux predicted with the local meteorological data, whatever the assumed shear velocity threshold. The remaining biases are probably due in part to the fact that the distribution of the ratios within the sections of U^*_{ERA} is not exactly Gaussian but we deem a more sophisticated statistical treatment not necessary.

4. Discussion–conclusion

Using the particular parameterization of the sand transport law proposed by White's, we found that the sand flux predicted based on the wind data is systematically lower than the mean sand flux of a single dune, Q_{Dunes}. The predicted sand flux is of the order of 65% Q_{Dunes} for a shear velocity threshold (impact threshold) $u_{*t} = 0.2612$ m/s estimated based on the local granulometric measurement using Shao and Lu's (2000) model. The agreement between the observed and predicted values is best for a shear velocity threshold close the minimum of 0.2346 m/s allowed by the model due to the inter-particle bonding by electrostatic forces, but the improvement is only marginal.

Several factors could explain the difficulty in reconciling the observed and predicted sand flux. Our mean sand flux prediction is sensitive to the Nikuradse parameter, which is not well constrained. Kok et al. (2012) implies that its value should be between D_p and $5D_p$, a broad range that impacts the final results (Fig. 7). We supposed, additionally, a parametrization of z_0 depending only on D_p (or u_{*t}), a case which is usually associated when no sand transport is observed (Bagnold, 1941). The effective aerodynamic roughness depends, however, also on the wind speed and increases when the shear velocity threshold is exceeded (Bagnold, 1941; Martin et al., 2013). Moreover, we took in this study a constant Von Karman parameter ($\kappa = 0.4$). It might actually vary with u_* (Li et al., 2010; Sherman and Li, 2012). The White (1979) transport law usually tend to overestimate observed sand flux and accounting for this non-constant Von Karman would slightly help correcting this bias (Sherman et al., 2013; Sherman and Li, 2012). However, our predictions with this law underestimate Q_{Dunes} and taking into account a variable Van Karman parameter would then worsen our predictions. In addition, other sand transport laws have been proposed in the literature that diverges from the u_*^3 proportionality of White's one (Ho et al., 2011; Kok et al., 2012). We are also neglecting the contribution of reptation to the sand transport flux. Since our maximum shear velocity, u_*, is at most 2 times larger than our minimum shear velocity threshold, u_{*t}, and according to Lammel et al. (2012), reptation could account for up to 50% of the flux from saltation. This means the flux due to reptation could account up to a third of the total flux. Neglecting all other bias, it is possible to estimate k_s fixing D_p and assuming that our estimated sand flux from satellite images is correct. In our study, we assume $k_s \approx \alpha D_p$, varying α from 1 to 5. Within this range our predicted sand flux from transport laws does not reconcile with the sand flux estimated from satellite observations (Fig. 7). A k_s value in excess of the largest values tested in this study would thus be needed but might be unreasonable. Additionally, the dunes in the field are not completely self-similar. They have a variety of shape which impacts directly our estimation of K (section 2.4) and thus Q_{Dunes}. For example small dunes do not generally possess any crest, contrarily to larger dunes. Similarly, interacting dunes are more difficult to characterize.

The effect of dune topography on the wind velocity profile could be a more likely cause for underestimating the dune sand flux. This might be due to the wind's acceleration on the dunes windward side (i.e. Momiji et al., 2000), an effect that is not accounted for as White's equation is supposing a flat surface. The crescent and asymmetrical shape of the barchans dunes might additionally help stabilize the wind direction and result in a more efficient sand transport than what our model predicts.

The procedure described in section 3.4 allows correcting the wind velocity predicted by ERA-Interim for the high frequency variations of wind velocity and the bias revealed by the comparison with the local meteorological data. We have seen that strong winds are slightly overestimated and weak winds are slightly underestimated. The extremely weak winds ($U^*_{ERA} < 0.05$ m s^{-1}), are strongly overestimated, but their contribution to the sand flux budget is negligible as they are significantly lower than the shear threshold velocity. Omitting these very weak winds, the relationship between R and U^*_{ERA} can be approximated by a linear equation $R = a * U^*_{ERA} + b$ with $a = 0.8039$ and $b = 0.7725$ from the comparison between the meteorological station raw data and U^*_{ERA}, and with $a = 1.163$ and $b = 0.6363$ for the comparison between U^*_{6h} and U^*_{ERA}. Similarly the standard deviation follows approximately $\sigma_R = cU^*_{ERA} + d$, with $c = -1.68$ and $d = 0.8171$ for the comparison between the meteorological station raw data and U^*_{ERA}, and with $c = -1.258$ and $d = 0.6179$ from the comparison between U^*_{6h} and U^*_{ERA}. To our knowledge, this bias has not been reported in previous studies. The physical reason of the bias are not clear. In reanalyses, the output is constrained by the assimilated data, but is also a result of the underlying model. Boundary layer processes are heavy parameterized and lower-level winds might hence have biases relative to more local observations. These trends are probably specific to the GCM and climatic setting of Qatar. Further investigations could explore how these trends would vary depending on the GCMs and local setting. The strategy described here can, however, be applied to any area where local wind measurements are available, including Mars. The Mars rover, Curiosity, has a wind mast and has collected data that could allow in principle correcting the wind velocity predicted by a Mars GCM following our procedure (Bridges et al., 2017; Newman et al., 2017; Silvestro et al., 2013).

Acknowledgements

This study has been partially funded by the King Abdullah City for Science and Technology. Essam Heggy is funded by the United States Agency for International Development (USAID) under the Further Advancing the Blue Revolution Initiative (FABRI-Grant#1001624-13S-19790). We thank Michel Louge for the meteorological station data in Qatar and for his comments and suggestions. Collection of local wind data was made possible by grant NPRP 6-059-2-023 from the Qatar National Research Fund. The Spot-5 images (Copyright CNES) were acquired through the ISIS program. The use of the Spot data was made possible by the grant Earthquakes without Frontiers (NE/M017559/1). We thank Giovanni Scabbia, Annamaria Mazzoni and Jonathan Normand for their help during the fieldwork. We thank Simona Bordoni for the insightful discussion and help regarding in particular the use of the GCM and ERA-Interim data.

Appendix A. Supplementary material

Supplementary material related to this article can be found online at https://doi.org/10.1016/j.epsl.2018.05.037.

References

Anderson, F.S., Greeley, R., Xu, P., Lo, E., Blumberg, D.G., Haberle, R.M., Murphy, J.R., 1999. Assessing the Martian surface distribution of aeolian sand using a Mars general circulation model. J. Geophys. Res., Planets 104, 18991–19002. https://doi.org/10.1029/1999JE900024.

Anderson, R.S., Sørensen, M., Willetts, B.B., 1991. Aeolian Grain Transport 1, 1st ed. Acta Mechanica Supplementum. Springer Vienna, Vienna.

Andreotti, B., 2004. A two-species model of aeolian sand transport. J. Fluid Mech. 510, 47–70. https://doi.org/10.1017/S0022112004009073.

Ayoub, F., Avouac, J.-P., Newman, C.E., Richardson, M.I., Lucas, A., Leprince, S., Bridges, N.T., 2014. Threshold for sand mobility on Mars calibrated from seasonal variations of sand flux. Nat. Commun. 5, 5096. https://doi.org/10.1038/ncomms6096.

Bagnold, R.A., 1941. The Physics of Blown Sand and Desert Dunes. Springer Netherlands, Dordrecht.

Barchyn, T.E., Martin, R.L., Kok, J.F., Hugenholtz, C.H., 2014. Fundamental mismatches between measurements and models in aeolian sediment transport prediction: the role of small-scale variability. Aeolian Res. 15, 245–251. https://doi.org/10.1016/j.aeolia.2014.07.002.

Bourke, M.C., Edgett, K.S., Cantor, B.A., 2008. Recent aeolian dune change on Mars. Geomorphology 94, 247–255. https://doi.org/10.1016/j.geomorph.2007.05.012.

Bridges, N.T., Ayoub, F., Avouac, J., Leprince, S., Lucas, A., Mattson, S., 2012. Earth-like sand fluxes on Mars. Nature 485, 339–342. https://doi.org/10.1038/nature11022.

Bridges, N.T., Sullivan, R., Newman, C.E., Navarro, S., van Beek, J., Ewing, R.C., Ayoub, F., Silvestro, S., Gasnault, O., Le Mouélic, S., Lapotre, M.G.A., Rapin, W., 2017. Martian aeolian activity at the Bagnold Dunes, Gale Crater: the view from the surface and orbit. J. Geophys. Res., Planets 122, 2077–2110. https://doi.org/10.1002/2017JE005263.

Butterfield, G.R., 1999. Near-bed mass flux profiles in aeolian sand transport: high-resolution measurements in a wind tunnel. Earth Surf. Process. Landf. 24, 393–412. https://doi.org/10.1002/(SICI)1096-9837(199905)24:5<393::AID-ESP996>3.0.CO;2-G.

Dee, D.P., Uppala, S.M., Simmons, A.J., Berrisford, P., Poli, P., Kobayashi, S., Andrae, U., Balmaseda, M.A., Balsamo, G., Bauer, P., Bechtold, P., Beljaars, A.C.M., van de Berg, L., Bidlot, J., Bormann, N., Delsol, C., Dragani, R., Fuentes, M., Geer, A.J., Haimberger, L., Healy, S.B., Hersbach, H., Hólm, E.V., Isaksen, L., Kållberg, P., Köhler, M., Matricardi, M., McNally, A.P., Monge-Sanz, B.M., Morcrette, J.-J., Park, B.-K., Peubey, C., de Rosnay, P., Tavolato, C., Thépaut, J.-N., Vitart, F., 2011. The ERA-Interim reanalysis: configuration and performance of the data assimilation system. Q. J. R. Meteorol. Soc. 137, 553–597. https://doi.org/10.1002/qj.828.

Durán, O., Parteli, E.J.R., Herrmann, H.J., 2010. A continuous model for sand dunes: review, new developments and application to barchan dunes and barchan dune fields. Earth Surf. Process. Landf. 35, 1591–1600. https://doi.org/10.1002/esp.2070.

Edgell, H.S., 2006. Arabian Deserts. Springer Netherlands, Dordrecht.

Embabi, N.S., Ashour, M.M., 1993. Barchan dunes in Qatar. J. Arid Environ. 25, 49–69. https://doi.org/10.1006/jare.1993.1042.

Ewing, R.C., Hayes, A.G., Lucas, A., 2015a. Sand dune patterns on Titan controlled by long-term climate cycles. Nat. Geosci. 8, 15–19. https://doi.org/10.1038/NGEO2323.

Ewing, R.C., McDonald, G.D., Hayes, A.G., 2015b. Multi-spatial analysis of aeolian dune-field patterns. Geomorphology 240, 44–53. https://doi.org/10.1016/j.geomorph.2014.11.023.

Garzanti, E., Vermeesch, P., Andò, S., Vezzoli, G., Valagussa, M., Allen, K., Kadi, K.A., Al-Juboury, A.I.A., 2013. Provenance and recycling of Arabian desert sand. Earth-Sci. Rev. 120, 1–19. https://doi.org/10.1016/j.earscirev.2013.01.005.

Génois, M., Courrech du Pont, S., Hersen, P., Grégoire, G., 2013. An agent-based model of dune interactions produces the emergence of patterns in deserts. Geophys. Res. Lett. 40, 3909–3914. https://doi.org/10.1002/grl.50757.

Greeley, R., Iversen, J.D., 1985. Wind as a Geological Process: on Earth, Mars, Venus and Titan. Cambridge University Press, New York.

Hersen, P., Andersen, K.H., Elbelrhiti, H., Andreotti, B., Claudin, P., Douady, S., 2004. Corridors of barchan dunes: stability and size selection. Phys. Rev. E, Stat. Nonlinear Soft Matter Phys. 69, 11304. https://doi.org/10.1103/PhysRevE.69.011304.

Ho, T.D., Valance, A., Dupont, P., Ould El Moctar, A., 2011. Scaling laws in aeolian sand transport. Phys. Rev. Lett. 106, 94501. https://doi.org/10.1103/PhysRevLett.106.094501.

Jackson, D.W.T., Bourke, M.C., Smyth, T.A.G., 2015. The dune effect on sand-transporting winds on Mars. Nat. Commun. 6, 8796. https://doi.org/10.1038/ncomms9796.

Kawamura, R., 1951. Study of Sand Movement by Wind. Hydraulic Engineering Laboratory Report HEL-2-8.

Kok, J.F., 2010. Difference in the wind speeds required for initiation versus continuation of sand transport on Mars: implications for dunes and dust storms. Phys. Rev. Lett. 104, 74502. https://doi.org/10.1103/PhysRevLett.104.074502.

Kok, J.F., Parteli, E.J.R., Michaels, T.I., Karam, D.B., Pierre, U., 2012. The physics of wind-blown sand and dust. Rep. Prog. Phys. 75. https://doi.org/10.1088/0034-4885/75/10/106901.

Kok, J.F., Renno, N.O., 2006. Enhancement of the emission of mineral dust aerosols by electric forces. Geophys. Res. Lett. 33, L19S10. https://doi.org/10.1029/2006GL026284.

Lambeck, K., 1996. Shoreline reconstructions for the Persian Gulf since the last glacial maximum. Earth Planet. Sci. Lett. 142, 43–57. https://doi.org/10.1016/0012-821X(96)00069-6.

Lammel, M., Rings, D., Kroy, K., 2012. A two-species continuum model for aeolian sand transport. New J. Phys. 14. https://doi.org/10.1088/1367-2630/14/9/093037.

Leprince, S., Barbot, S., Ayoub, F., Avouac, J., 2007. Automatic and precise orthorectification, coregistration, and subpixel correlation of satellite images, application to ground deformation measurements. IEEE Trans. Geosci. Remote Sens. 45, 1529–1558. https://doi.org/10.1109/TGRS.2006.888937.

Li, B., Sherman, D.J., Farrell, E.J., Ellis, J.T., 2010. Variability of the apparent von Kármán parameter during aeolian saltation. Geophys. Res. Lett. 37. https://doi.org/10.1029/2010GL044068.

Lorenz, R.D., 2006. The sand seas of Titan: Cassini RADAR observations of longitudinal dunes. Science 312, 724–727. https://doi.org/10.1126/science.1123257.

Louge, M.Y., Valance, A., Mint Babah, H., Moreau-Trouvé, J.-C., Ould el-Moctar, A., Dupont, P., Ould Ahmedou, D., 2010. Seepage-induced penetration of water vapor and dust beneath ripples and dunes. J. Geophys. Res., Earth Surf. 115. https://doi.org/10.1029/2009JF001385.

Louge, M.Y., Valance, A., el-Moctar, A.O., Xu, J., Hay, A.G., Richer, R., 2013. Temperature and humidity within a mobile barchan sand dune, implications for microbial survival. J. Geophys. Res., Earth Surf. 118 (4), 2392–2405.

Martin, R.L., Barchyn, T.E., Hugenholtz, C.H., Jerolmack, D.J., 2013. Timescale dependence of aeolian sand flux observations under atmospheric turbulence. J. Geophys. Res., Atmos. 118, 9078–9092. https://doi.org/10.1002/jgrd.50687.

Martin, R.L., Kok, J.F., 2017. Wind-invariant saltation heights imply linear scaling of aeolian saltation flux with shear stress. Sci. Adv. 3, e1602569. https://doi.org/10.1126/sciadv.1602569.

McDonald, G.D., Hayes, A.G., Ewing, R.C., Lora, J.M., Newman, C.E., Tokano, T., Lucas, A., Soto, A., Chen, G., 2016. Variations in Titan's dune orientations as a result of orbital forcing. Icarus 270, 197–210. https://doi.org/10.1016/j.icarus.2015.11.036.

Momiji, H., Carretero-Gonzalez, R., Bishop, S.R., Warren, A., 2000. Simulation of the effect of wind speedup in the formation of transverse dune fields. Earth Surf. Process. Landf. 25, 905–918. https://doi.org/10.1002/1096-9837(200008)25:8<905::AID-ESP112>3.0.CO;2-Z.

Newman, C.E., Gómez-Elvira, J., Marin, M., Navarro, S., Torres, J., Richardson, M.I., Battalio, J.M., Guzewich, S.D., Sullivan, R., de la Torre, M., Vasavada, A.R., Bridges, N.T., 2017. Winds measured by the Rover Environmental Monitoring Station (REMS) during the Mars Science Laboratory (MSL) rover's Bagnold Dunes Campaign and comparison with numerical modeling using MarsWRF. Icarus 291, 203–231. https://doi.org/10.1016/j.icarus.2016.12.016.

Nikuradse, J., 1933. Stromungsgesetz in rauhren Rohren. VDI Forschungshefte 361 (English translation: Laws of Flow in Rough Pipes). Tech. Rep. NACA Tech. Memo. 1292. Natl. Advis. Comm. Aeronaut.

Ould Ahmedou, D., Mahfoudh, A.O., Dupont, P., El Moctar, A.O., Valance, A., Rasmussen, K.R., 2007. Barchan dune mobility in Mauritania related to dune and interdune sand fluxes. J. Geophys. Res. 112. https://doi.org/10.1029/2006JF000500.

Shao, Y., Lu, H., 2000. A simple expression for wind erosion threshold friction velocity. J. Geophys. Res., Atmos. 105, 22437–22443. https://doi.org/10.1029/2000JD900304.

Sherman, D.J., Houser, C., Ellis, J.T., Farrell, E.J., Li, B., Davidson-Arnott, R.G.D., Baas, A.C.W., Maia, L.P., 2013. Characterization of aeolian streamers using time-average videography. J. Coast. Res. 165, 1331–1336. https://doi.org/10.2112/SI65-225.1.

Sherman, D.J., Li, B., 2012. Predicting aeolian sand transport rates: a reevaluation of models. Aeolian Res. 3, 371–378. https://doi.org/10.1016/j.aeolia.2011.06.002.

Silvestro, S., Vaz, D.A., Ewing, R.C., Rossi, A.P., Fenton, L.K., Michaels, T.I., Flahaut, J., Geissler, P.E., 2013. Pervasive aeolian activity along rover curiosity's traverse in Gale, Mars. Geology 41, 483–486. https://doi.org/10.1130/G34162.1.

Sullivan, R., Kok, J.F., 2017. Aeolian saltation on Mars at low wind speeds. J. Geophys. Res., Planets 122, 2111–2143. https://doi.org/10.1002/2017JE005275.

Tsoar, H., Greeley, R., Peterfreund, A.R., 1979. MARS: the North Polar Sand Sea and related wind patterns. J. Geophys. Res. 84, 8167. https://doi.org/10.1029/JB084iB14p08167.

White, B.R., 1979. Soil transport by winds on Mars. J. Geophys. Res. 84, 4643. https://doi.org/10.1029/JB084iB09p04643.

White, F.M., 2006. Viscous Fluid Flow. McGraw–Hill Education, N.Y., 3rd ed.

Yizhaq, H., Kok, J.F., Katra, I., 2014. Basaltic sand ripples at Eagle crater as indirect evidence for the hysteresis effect in Martian saltation. Icarus 230, 143–150.

York, D., Evensen, N.M., Martínez, M.L., De Basabe Delgado, J., 2004. Unified equations for the slope, intercept, and standard errors of the best straight line. Am. J. Phys. 72, 367–375. https://doi.org/10.1119/1.1632486.

Zhang, D., Yang, X., Rozier, O., Narteau, C., 2014. Mean sediment residence time in barchan dunes. J. Geophys. Res., Earth Surf. 119 (3), 451–463.